ROYAL SOCIETY OF CHEMISTRY

PAPER

Check for updates

High-efficiency ammonia electrosynthesis from nitrate on ruthenium-induced trivalent cobalt sites†

Longcheng Zhang, [ab] Yuan Liu,[b] Ling Li,[c] Tianze Wu,[b] Qian Wu,[b] Justin Zhu Yeow Seow,[b] Xiu Lin,[b] Shirong Sun,[b] Leonhard Tannesia,[b] Kai Tang,[b] Dongsheng Shao,[b] Shibo Xi,[d] Xiaodong Guo *[a] and Zhichuan J. Xu*[be]

Electrocatalytic nitrate reduction to ammonia holds significant potential for sustainable ammonia production and nitrate-rich wastewater treatment. However, the low catalytic efficiency and limited understanding of catalyst evolution hinder its further advancement, particularly at low nitrate concentrations. Here, we report a Ru-doped Co(OH)$_2$ nanoarray that achieves a high ammonia faradaic efficiency of $\sim$96% and a large ammonia yield rate of $\sim$56 501 µg h^{-1} cm$_{geo}^{-2}$ at -0.48 V *versus* reversible hydrogen electrode under wastewater-relevant nitrate concentrations. *Ex situ* X-ray absorption spectroscopy and X-ray diffraction measurements reveal the dynamic redox behavior of Co(II)/Co(III) sites, driven by Ru-catalyzed hydroxide oxidation and electroreduction. Mechanistic insights from *in situ* Raman spectroscopy and electron paramagnetic resonance spectroscopy indicate that Ru doping generates more hydrogen radicals, thus facilitating the formation of intermediate HNO species at Co(III) sites. Additionally, the practical applicability and economic feasibility of electrocatalytic nitrate reduction to ammonia are underscored by an integrated membrane electrode assembly system and a techno-economic analysis.

Broader context
Electrocatalytic nitrate reduction offers a sustainable alternative to conventional ammonia production while addressing nitrate pollution in wastewater. However, most research to date has focused on high nitrate concentrations, leaving a significant gap in understanding the structural evolution of catalysts and the underlying reaction mechanisms under wastewater-relevant conditions. This study presents a ruthenium-doped cobalt hydroxide catalyst that achieves a remarkable ammonia faradaic efficiency of $\sim$96% and a large ammonia yield rate of $\sim$56 501 µg h^{-1} cm$_{geo}^{-2}$ at wastewater-relevant nitrate concentrations. By leveraging advanced spectroscopic techniques, the work provides fundamental insights into the dynamic redox behavior of Co(II)/Co(III) sites and the role of Ru in enhancing hydrogen radical generation, which facilitates nitrate-to-ammonia conversion. Additionally, the study underscores the practical viability of this approach through an integrated membrane electrode assembly system and a techno-economic analysis, bridging the gap between fundamental research and real-world implementation.

Introduction

Ammonia (NH$_3$), with an annual global demand exceeding 150 million tonnes, serves as an essential foundation for

a School of Chemical Engineering, Sichuan University, Chengdu, 610065, China. E-mail: xiaodong2009@scu.edu.cn
b School of Materials Science and Engineering, Nanyang Technological University, Singapore, 639798, Singapore. E-mail: xuzc@ntu.edu.sg
c Analytical & Testing Centre, Sichuan University, Chengdu, 610064, China
d Institute of Sustainability for Chemicals, Energy and Environment (ISCE²), Agency for Science, Technology and Research (A*STAR), Singapore, 627833, Singapore
e Centre for Advanced Catalysis Science and Technology, Nanyang Technological University, Singapore, 639798, Singapore
† Electronic supplementary information (ESI) available. See DOI: https://doi.org/10.1039/d5ee01585e

nitrogen fertilizer production and is considered as a promising carbon-free energy carrier for a sustainable future.[1–3] Industrial NH$_3$ synthesis is driven by the Haber–Bosch process, an energy-intensive approach that relies on hydrogen feedstock and contributes significantly to greenhouse gas emissions, making it environmentally unsustainable.[4,5] In contrast, the electrochemical nitrogen reduction reaction offers a promising alternative to the conventional Haber–Bosch process but is hindered by a low faradaic efficiency (FE) and limited NH$_3$ yield rate, primarily due to the high bond energy of the N$\equiv$N bond (941 kJ mol^{-1}).[6–9] Nitrate (NO$_3^-$), a prevalent pollutant in industrial and agricultural wastewater, represents a more accessible target for reduction owing to its high solubility and low bond energy of the N=O bond (204 kJ mol^{-1}).[10–12] Although substantial advancements have been made in the development

5622 | *Energy Environ. Sci.*, 2025, **18**, 5622–5631

This journal is © The Royal Society of Chemistry 2025

of efficient catalysts for the electrochemical NO_3^- reduction reaction (NO_3RR),[13–17] these studies have predominantly been conducted at high NO_3^- concentrations (≥ 0.1 M), where competing reactions are minimized. In fact, practical NO_3^- sources, including industrial wastewater and polluted groundwater, often exhibit low NO_3^- concentrations ranging from hundreds to thousands of ppm.[18,19] Therefore, the development of highly active electrocatalysts capable of achieving exceptional NH_3 yield rates and FEs from low-concentration NO_3^- remains a critical challenge.

Cobalt-based electrocatalysts, particularly cobalt hydroxide, are recognized as active and selective candidates for the NO_3RR, owing to cobalt's abundant vacant sp^3 orbitals that enhance NO_3^- adsorption.[20–25] Notably, cobalt hydroxide often undergoes dynamic structural evolution along with the changes of the applied potential. Luo et al. demonstrated that a metallic Co nanoarray derived from cobalt hydroxide exhibits excellent NO_3^- reduction activity, attributed to Co enhancing interactions between the surface-adsorbed *H_2O and nucleophilic *N, *NH, and *NH_2 species.[23] Pan et al. further revealed that precise control over the reconstruction of cobalt hydroxide can significantly enhance both activity and stability in the NO_3RR.[24] However, the structural evolution of cobalt-based catalysts and the identification of Co active sites in the NO_3RR remain controversial. While surface reconstructions of electrocatalysts have been widely reported,[26–29] the dynamic structural evolution and reaction mechanisms in the NO_3RR, especially at low NO_3^- concentrations, remain poorly understood, yet are crucial.

Herein, we report a high-performance Ru-doped $Co(OH)_2$ nanosheet electrocatalyst on carbon cloth (Ru–$Co(OH)_2$/CC) for the NO_3RR, achieving a large NH_3 yield rate of $\sim 56\,501$ $\mu g\ h^{-1}\ cm_{geo}^{-2}$ and a high FE of $\sim 96\%$ at low NO_3^- concentrations. Ex situ X-ray absorption spectroscopy (XAS) and X-ray diffraction (XRD) studies elucidate the dynamically existing Co(III) sites on the Ru–$Co(OH)_2$ surface during the NO_3RR. In situ Raman spectroscopy and electron paramagnetic resonance (EPR) spectroscopy results confirm that the enhanced generation of hydrogen radicals at Ru sites promotes a more efficient conversion of NO_3^- into HNO* intermediates at Co(III) sites. Additionally, we demonstrate the successful conversion of NO_3^- into practical NH_3 products with a nearly unchanged FE ($> 90\%$) in a membrane electrode assembly (MEA) system. A preliminary techno-economic assessment (TEA) underscores the economic viability of producing NH_3 through the NO_3RR, further highlighting its potential for scalable applications.

Results and discussion

Synthesis and characterization

Ru–$Co(OH)_2$/CC was synthesized through a two-step procedure of electrodeposition followed by an ion-exchange process (see methods for details). The XRD patterns of $Co(OH)_2$/CC and Ru-x-$Co(OH)_2$/CC ($x = 0.2, 1, 5,$ and 10, where x denotes the $RuCl_3$ solution concentration in mM) are shown in Fig. 1a. Both $Co(OH)_2$/CC and Ru-x-$Co(OH)_2$/CC exhibit the characteristic crystal structure of α-$Co(OH)_2$, with NO_3^- serving as

the interlayer anion.[30] No diffraction peaks corresponding to Ru species (such as Ru or RuO_2) are observed. Scanning electron microscopy (SEM) images of Ru-x-$Co(OH)_2$/CC (Fig. S1, ESI†) show the uniform growth of densely arranged nanosheets across the CC substrate. Similarly, transmission electron microscopy (TEM) analysis (Fig. S2, ESI†) highlights the presence of ultrathin nanosheets, confirming that the $Co(OH)_2$ nanosheet morphology is preserved after the cation exchange process. Cyclic voltammetry (CV) curves for pristine and cycled $Co(OH)_2$/CC and Ru-x-$Co(OH)_2$/CC, collected in Ar-saturated 1 M KOH containing 2000 ppm NO_3^-, are shown in Fig. S3 (ESI†). Although $Co(OH)_2$/CC shows a decrease in current density after the 2nd cycle, Ru-x-$Co(OH)_2$/CC maintains an increased current density after the 1st cycle. All Ru-x-$Co(OH)_2$/CC samples show a higher current density in the 100th cycle than in the 1st cycle (Fig. 1b), indicating substantial reconstruction, with the optimal enhancement observed at $x = 5$. Ru-5-$Co(OH)_2$/CC achieves the lowest potentials of 163, 246, and 415 mV at 100, 200, and 400 mA cm^{-2}, respectively, after 100 CV cycles (Fig. 1c). Furthermore, the activity enhancement for Ru-x-$Co(OH)_2$/CC remains minor in the absence of NO_3^- (Fig. S4, ESI†). Characterization of Ru-5-$Co(OH)_2$/CC before and after CV cycling was conducted to evaluate structural transformations. The XRD patterns of Ru-5-$Co(OH)_2$/CC before and after CV cycling display characteristic peaks of α-$Co(OH)_2$ and β-$Co(OH)_2$ in the early stages, with these phases fully transitioning to the β-$Co(OH)_2$ phase after the 50th cycle in Ar-saturated 1 M KOH solution containing 2000 ppm NO_3^- (Fig. S5, ESI†). A phase of CoO(OH) (JCPDS No. 72-2280) appeared as early as the 10th CV cycle for Ru-5-$Co(OH)_2$/CC, while no such phase was observed for $Co(OH)_2$/CC during CV cycling (Fig. S6, ESI†). High-resolution TEM (HRTEM) images revealed a new crystal lattice with a spacing of 0.242 nm, corresponding to CoO(OH) (100), in Ru-5-$Co(OH)_2$/CC after the 10th CV cycle in Ar-saturated 1 M KOH solution containing 2000 ppm NO_3^- (Fig. 1d). SEM and the related elemental mapping images confirm that Ru-5-$Co(OH)_2$ nanosheet arrays remain intact after the 10th CV cycle (Fig. S7, ESI†). X-ray absorption near-edge structure (XANES) analysis at the Co K-edge was performed to explore the electronic states of Co in Ru-5-$Co(OH)_2$/CC. Fig. 1e shows that the absorption edge shifts to a higher energy from the pristine Ru-5-$Co(OH)_2$/CC to the 10th cycled Ru-5-$Co(OH)_2$/CC, indicating an increase in the Co oxidation state.[31–33] With increasing CV cycles, although the absorption edge gradually shifts back to lower energy, it remains higher than that of the pristine material, which indicates a dynamic evolution of the Co oxidation state during cycling. Fig. S8 (ESI†) further shows a consistent shift in the absorption edge towards the lower wavelength regime as the number of cycles increases, suggesting a progressive decrease in the Co oxidation state of $Co(OH)_2$/CC during the NO_3RR. To offer comprehensive insights into the R- and k-space, wavelet transform (WT) analysis was applied to the extended X-ray absorption fine structure (EXAFS) spectra, as shown in Fig. 1f. The WT contour plot of Ru-5-$Co(OH)_2$/CC before and after CV cycling exhibits two intensity maxima at approximately 5.0 Å^{-1} and 7.1 Å^{-1}, attributed to the Co–O and Co–Co contributions, respectively.[34–36]

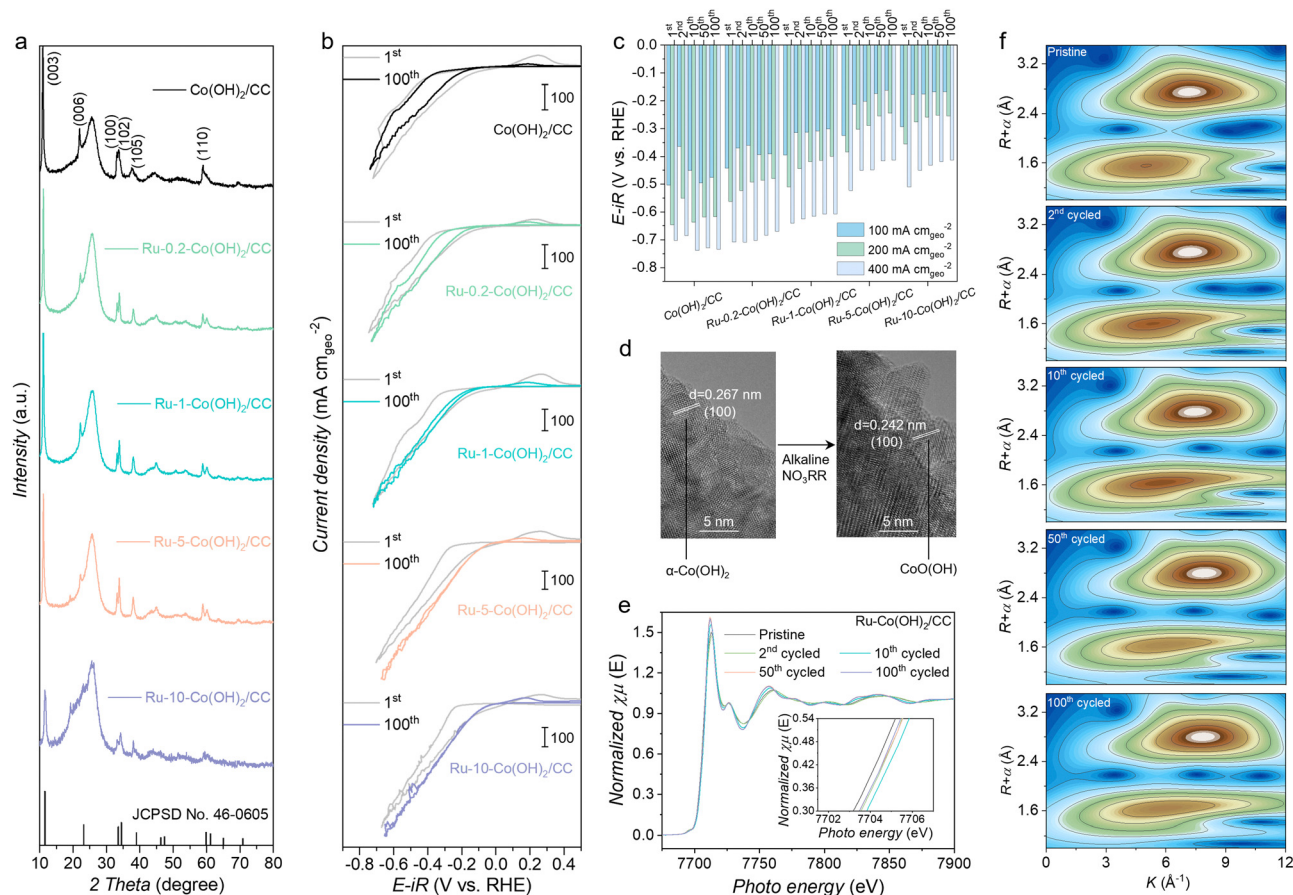This journal is © The Royal Society of Chemistry 2025

Energy Environ. Sci., 2025, **18**, 5622–5631 | **5623**

Fig. 1 Phase transitions on Ru–Co(OH)$_2$/CC during the NO$_3$RR. (a) XRD patterns of Co(OH)$_2$/CC and Ru-x-Co(OH)$_2$/CC. (b) CV curves of Co(OH)$_2$/CC and Ru-x-Co(OH)$_2$/CC in Ar-saturated 1 M KOH solution containing 2000 ppm NO$_3^-$ with a scan rate of 50 mV s^{-1}. (c) Potential comparison of different current densities. (d) HRTEM images of pristine Ru-5-Co(OH)$_2$/CC and the 10th cycled Ru-5-Co(OH)$_2$/CC. (e) Normalized Co K-edge XANES spectra and (f) WT-EXAFS plots of the pristine and cycled Ru-5-Co(OH)$_2$/CC.

Notably, after CV cycling, the Co–O path shows a slight shift to higher k-space in the WT contour plots, which is attributed to the incorporation of O in the first coordination shell of Co atoms.[35] Based on these results, the phase translation hypothesis for Ru–Co(OH)$_2$/CC during the NO$_3$RR is summarized in Fig. S9 (ESI†).

Electrochemical NO$_3$RR performance

The synthesized samples were evaluated for the NO$_3$RR in an Ar-saturated 1 M KOH solution with or without the NO$_3^-$ electrolyte. A NO$_3^-$ concentration of 2000 ppm, which is representative of industrial wastewater levels, was employed in the electrolyte.[37] All linear sweep voltammetry (LSV) curves were obtained after repeated CV cycling until stabilization, ensuring the complete phase transition of materials. The LSV curve of Ru–Co(OH)$_2$/CC exhibits superior NO$_3$RR performance, with a large current density (Fig. 2a). EIS analysis confirmed that Ru–Co(OH)$_2$/CC exhibited minimal charge transfer resistance, signifying its high efficiency in electron transfer (Fig. S10, ESI†). Ru–Co(OH)$_2$/CC also exhibits an enhanced electrochemical active surface area (ECSA) (Fig. S11, ESI†), as evidenced by the double-layer capacitance obtained from cyclic

voltammograms, indicating that Co(OH)$_2$ nanosheets doped with Ru process the maximum reactive area.[38] Moreover, the ECSA-normalized current density of Ru–Co(OH)$_2$/CC was higher than that of Co(OH)$_2$/CC (Fig. S12, ESI†), indicating that the superior NO$_3$RR performance arises from an intrinsic activity induced by Ru doping rather than an enlarged surface area.[39] A NO$_3$RR performance comparison of Ru–Co(OH)$_2$/CC prepared using RuCl$_3$ solution concentrations of 0.2, 1, 5, and 10 mM during the ion-exchange process was systematically conducted. Among the tested samples, Ru-5-Co(OH)$_2$/CC exhibited the lowest Tafel slope of 145.2 mV dec^{-1} (Fig. S13, ESI†), indicating the most efficient electron transfer kinetics during the NO$_3$RR. The enhanced NO$_3$RR activity of Ru-5-Co(OH)$_2$/CC is also attributed to its reduced charge transfer resistance, as demonstrated in Fig. S14. In this study, NH$_3$, NO$_2^-$, and residual NO$_3^-$ were quantified using UV-vis spectrophotometry (Fig. S15–S17, ESI†). As shown in Fig. S18 (ESI†), Ru-5-Co(OH)$_2$/CC maintained high NH$_3$ yield rates and FEs across a wide potential range, outperforming other Ru-x-Co(OH)$_2$/CC electrodes. Consequently, a 5 mM ion-exchange concentration was selected as the optimal synthesis condition. A control sample of commercial Ru nanoparticles on carbon cloth (Ru/CC) was also
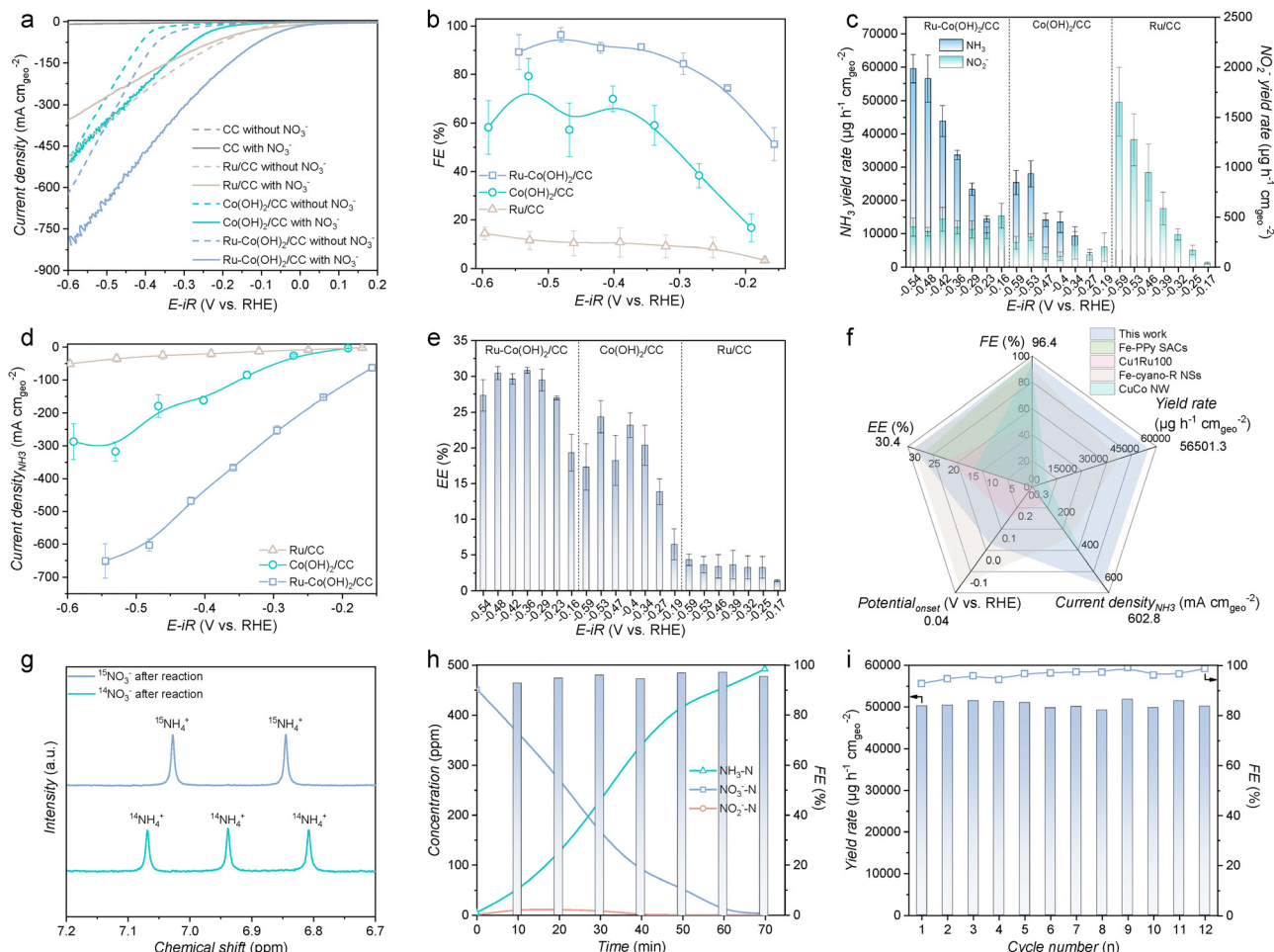
5624 | *Energy Environ. Sci.*, 2025, **18**, 5622–5631

This journal is © The Royal Society of Chemistry 2025

Fig. 2 Electrocatalytic NO$_3$RR performance. (a) Polarization curves of Ru–Co(OH)$_2$/CC, Co(OH)$_2$/CC, Ru/CC, and CC measured with and without 2000 ppm NO$_3^-$ in Ar-saturated 1 M KOH solution. (b) FEs of NH$_3$ and the (c) yield rates of NH$_3$ and NO$_2^-$ for Ru–Co(OH)$_2$/CC, Co(OH)$_2$/CC, and Ru/CC. (d) Partial current densities and (e) energy efficiency of NH$_3$ for Ru–Co(OH)$_2$/CC, Co(OH)$_2$/CC, and Ru/CC. (f) Comparison of NO$_3$RR performance over Ru–Co(OH)$_2$/CC with recently reported catalysts. (g) NMR spectra of the products generated during the NO$_3$RR with Ru–Co(OH)$_2$/CC in Ar-saturated 1 M KOH with 2000 ppm K^{15}NO$_3$ or 2000 ppm K^{14}NO$_3$ at −0.48 V $vs.$ RHE. (h) The time-dependent concentration of NO$_3^-$, NO$_2^-$, and NH$_3$ over Ru–Co(OH)$_2$/CC at −0.48 V $vs.$ RHE. (i) NH$_3$ yield rates and FEs on Ru–Co(OH)$_2$/CC under the potential of −0.48 V $vs.$ RHE during 12 periods of the 30-min NO$_3$RR.

characterized (Fig. S19, ESI†). Additional samples with alternative noble metal dopants, including Pd, Ir, and Rh, were also prepared and characterized (Fig. S20–S22, ESI†). As shown in Fig. S23 and S24 (ESI†), Ru–Co(OH)$_2$/CC consistently outperformed Pd–Co(OH)$_2$/CC, Ir–Co(OH)$_2$/CC, and Rh–Co(OH)$_2$/CC in terms of the current density, NH$_3$ yield rate, and NH$_3$ FE. Fig. 2b shows the potential-dependent NH$_3$ FEs obtained for Ru–Co(OH)$_2$/CC, Co(OH)$_2$/CC, and Ru/CC. Remarkably, Ru–Co(OH)$_2$/CC achieved a maximum NH$_3$ FE of ∼96% at −0.48 V and sustained a high FE across a broad potential window, significantly outperforming Co(OH)$_2$/CC. The NH$_3$ yield rates shown in Fig. 2c further demonstrate the enhanced NH$_3$ yield rate of Ru–Co(OH)$_2$/CC. With increasingly negative applied potentials, Ru–Co(OH)$_2$/CC delivered a high NH$_3$ yield rate of ∼56 501 μg h^{-1} cm$_{geo}^{-2}$ with a large NH$_3$ partial current density of −602.8 mA cm$_{geo}^{-2}$ at −0.48 V $vs.$ RHE, outperforming Co(OH)$_2$/CC (27 857.3 μg h^{-1} cm$_{geo}^{-2}$) and

Ru/CC (3244.3 μg h^{-1} cm$_{geo}^{-2}$) (Fig. 2d). The onset potential and half-cell energy efficiency (EE) of Ru–Co(OH)$_2$/CC were 0.04 V $vs.$ RHE and 30.4%, respectively, both significantly more favorable than those of Co(OH)$_2$/CC (−0.15 V $vs.$ RHE and 24.3%) and Ru/CC (−0.08 V $vs.$ RHE and 3.5%) (Fig. 2e and Fig. S25, ESI†). The key performance parameters are summarized in Fig. 2f and Table S1 (ESI†), alongside comparisons with recent reports. To eliminate the potential interference from the electrocatalyst or external environment, we performed isotope-labeling experiments using ^{15}N-labeled NO$_3^-$ as the reagent. Unlike ^{14}NH$_4^+$, which exhibited three peaks in the ^{1}H NMR spectra, only the characteristic doublet peaks of ^{15}NH$_4^+$ were observed when ^{15}NO$_3^-$ was used as the nitrogen source (Fig. 2g). This result confirms that NH$_3$ production resulted from NO$_3^-$ in the electrolyte. The NMR-derived ^{14}NH$_3$ yield rates were consistent with UV-vis results (Fig. S26, ESI†), confirming the reliability of the quantification methods. To demonstrate the broad adaptability of

This journal is © The Royal Society of Chemistry 2025

Energy Environ. Sci., 2025, **18**, 5622–5631 | **5625**

Ru–Co(OH)$_2$/CC, we evaluated its performance across a range of NO$_3^-$ concentrations. In addition to the 2000 ppm (32.3 mM) level, we selected 10 mM and 100 mM NO$_3^-$ to represent typical NO$_3^-$ concentrations found in household wastewater and heavy industrial effluents, respectively. Remarkably, Ru–Co(OH)$_2$/CC achieved impressive NH$_3$ FEs of 85.8% and 98.9% in an Ar-saturated 1 M KOH solution containing 10 mM and 100 mM NO$_3^-$, respectively (Fig. S27, ESI†). Moreover, the catalytic activity of the Ru–Co(OH)$_2$/CC under the neutral conditions was further evaluated. Such Ru–Co(OH)$_2$/CC exhibited a comparable NH$_3$ yield rate (7279.07 µg h^{-1} cm$_{geo}^{-2}$) and FE (88.5%) to that of under the alkaline conditions (Fig. S28, ESI†). To assess its practical viability, the NO$_3^-$ removal capacity in simulated wastewater containing 2000 ppm NO$_3^-$ was evaluated (Fig. 2h and Fig. S29, ESI†). Notably, NO$_3^-$ and NO$_2^-$ were reduced to levels below the World Health Organization drinking water standards within 70 min, while maintaining the NH$_3$ FE above 90%, demonstrating excellent NO$_3^-$ wastewater treatment capabilities.[40] This rapid and efficient reduction highlights the potential of Ru–Co(OH)$_2$/CC for real-world applications in wastewater treatment. Furthermore, the durability of Ru–Co(OH)$_2$/CC for the NO$_3$RR was confirmed through consecutive electrolysis cycles. As shown in Fig. 2i, the NH$_3$ yield rates and FEs were consistently maintained over 12 cycles, indicating good stability. XRD, high-resolution X-ray photoelectron spectroscopy, SEM, and TEM analyses further demonstrated the high stability of Ru–Co(OH)$_2$/CC during the NO$_3$RR (Fig. S30–S33, ESI†).

Reaction mechanism analysis

To analyze the properties of electrode/electrolyte interfaces during the NO$_3$RR, *operando* EIS measurements were performed at different potentials. As shown in Fig. S34 (ESI†), the cathodic resistance comprises four components. The generation of H* *via* water dissociation (Volmer step) occurs in the low-frequency range ($<10^0$ Hz), whereas the subsequent consumption of H* (Heyrovsky step) occurs in the middle-frequency range (10^0 to 10^2 Hz).[41] The charge-transfer resistance observed in the Nyquist plots of Ru–Co(OH)$_2$/CC is smaller than that of Co(OH)$_2$/CC under the same bias, indicating that Ru–Co(OH)$_2$/CC exhibits a faster charge transfer rate during the NO$_3$RR (Fig. S35, ESI†).[42] As reported, the phase angle provides insights into the proportion of charges participating in the catalytic process, where smaller phase angles indicate a higher involvement of charges in the faradaic process.[43] The peak intensities of Ru–Co(OH)$_2$/CC are lower than those of Co(OH)$_2$/CC and shift to much lower frequencies from 0.1 to -0.4 V *vs.* RHE (Fig. 3a and b). This shift confirms that Ru doping not only slows the Heyrovsky step but also inhibits H$_2$ generation,[44] enabling more efficient capture of H* by NO$_3^-$ for NH$_3$ formation. As shown in Fig. 3c, within the potential window of 0.3 to -0.4 V *vs.* RHE, the smaller phase angles of Ru–Co(OH)$_2$/CC in the middle-frequency region (around 10^1 to 10^2 Hz) demonstrate enhanced charge transfer and fast NO$_3$RR kinetics, directly attributable to the effect of Ru doping.[45] Further insights were obtained using quasi EPR spectroscopy to investigate the generation and consumption of hydrogen radicals during the

NO$_3$RR. As shown in Fig. 3d, after electrolysis in Ar-saturated 1 M KOH solution, Ru–Co(OH)$_2$/CC exhibits significantly stronger DMPO–H signals than Co(OH)$_2$/CC, indicating that Ru–Co(OH)$_2$/CC favors water dissociation and promotes the formation of active hydrogen necessary for protonation. While Co(OH)$_2$/CC exhibited slightly reduced DMPO–H signals, nearly all DMPO–H signals for Ru–Co(OH)$_2$/CC disappeared, suggesting the rapid consumption of hydrogen radicals on Ru–Co(OH)$_2$/CC to enhance NO$_3$RR hydrogenation energetics. The open-circuit potential (OCP), which reflects changes in absorbates within the Helmholtz layer, was measured to evaluate the NO$_3^-$ adsorption behavior (Fig. 3e).[46] A significant decrease in the OCP ($\sim$50.1 mV) was observed for Ru–Co(OH)$_2$/CC after adding 2000 ppm NO$_3^-$, compared to that for Co(OH)$_2$/CC ($\sim$0.6 mV), indicating that Ru doping enhances NO$_3^-$ adsorption on the catalyst. To investigate surface phase evolution, *in situ* Raman spectroscopy was conducted at various applied potentials (Fig. S36, ESI†). For Ru–Co(OH)$_2$/CC (Fig. 3f), the stretching vibration peak at 527 cm^{-1}, attributed to Co(OH)$_2$, was observed. At -0.2 V *vs.* RHE, a new peak at 509 cm^{-1}, corresponding to CoO(OH), appeared, suggesting partial oxidation of Co^{2+} to Co^{3+}.[47,48] In contrast, the Raman spectra of Co(OH)$_2$/CC showed no CoO(OH)-related peaks, with the Co(OH)$_2$ peak at 527 cm^{-1} remaining unchanged across applied potentials (Fig. 3g). Additionally, the Raman peaks at 688 cm^{-1}, corresponding to the Co–O vibration, diminished with increasingly negative potentials (0 V to -0.9 V *vs.* RHE). This phenomenon was also observed in Ar-saturated 1 M KOH solution (Fig. S37, ESI†). However, for Ru–Co(OH)$_2$/CC, the Co(OH)$_2$ peak at 688 cm^{-1} disappeared after immersion in Ar-saturated 1 M KOH solution with 2000 ppm NO$_3^-$, accompanied by the emergence of a CoO(OH) peak at 509 cm^{-1}. No CoO(OH) peaks were observed for Co(OH)$_2$/CC under similar conditions, implying that Ru promotes Co(OH)$_2$ oxidation in the presence of high OH$^-$ concentrations (Fig. S38, ESI†). A peak at 1060 cm^{-1}, corresponding to the symmetric stretching vibration of NO$_3^-$, was present across applied potentials (Fig. 3f and g).[49] Additionally, a peak at 1554 cm^{-1}, attributed to the N–O stretch of HNO, emerged as the potential shifted negatively to -0.9 V *vs.* RHE.[50] As shown in Fig. 3h and Table S2 (ESI†), the intensity ratio of the peak at 1060 cm^{-1} and 1554 cm^{-1} (I_{1060}/I_{1554}) for Ru–Co(OH)$_2$/CC was consistently lower than that of Co(OH)$_2$/CC across the potential range of -0.2 to -0.9 V *vs.* RHE, indicating more efficient conversion of NO$_3^-$ to the HNO species. As shown in Fig. 3i, Ru sites facilitate the generation of hydrogen radicals during the NO$_3$RR, thereby providing sufficient protons for NO$_3^-$ hydrogenation. Concurrently, under the influence of Ru, the neighboring Co(OH)$_2$ is oxidized by the OH$^-$ to form high-valence CoO(OH) (Co(OH)$_2$ + OH$^-$ → CoO(OH) + H$_2$O + e$^-$), which serves as an active site for converting NO$_3^-$ to the HNO species. This synergistic interaction between Ru and CoO(OH) ultimately facilitates efficient NH$_3$ synthesis.

Theoretical simulations

We further employed density functional theory (DFT) calculations to investigate the improved NO$_3$RR performance of the Ru–Co(OH)$_2$ catalyst by constructing a Ru–Co(OH)$_2$ model (Fig. 4a).

5626 | *Energy Environ. Sci.*, 2025, **18**, 5622–5631
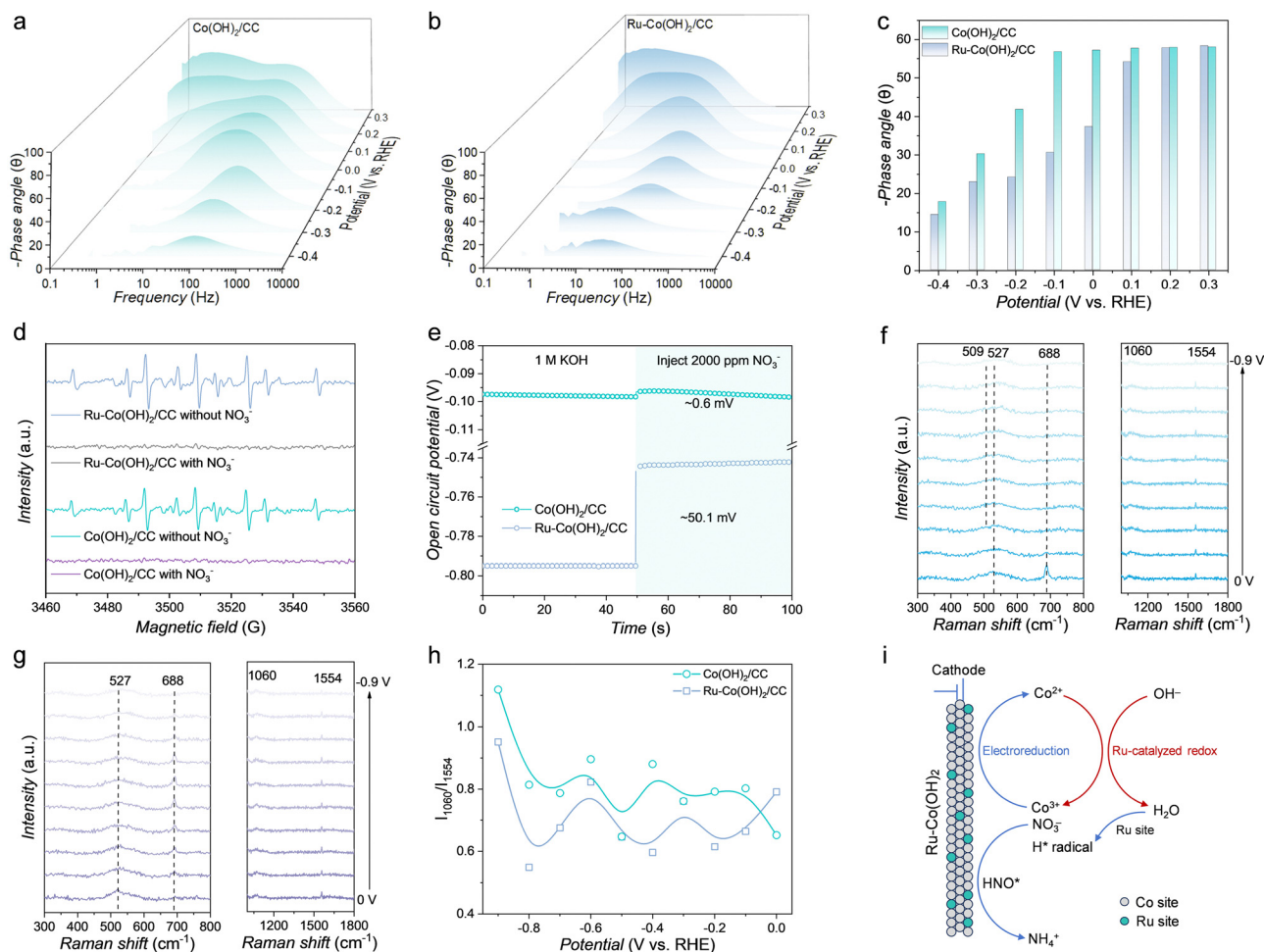
This journal is © The Royal Society of Chemistry 2025

Fig. 3 *Operando* characterization and the mechanism of the phase transition. Bode phase plots of (a) $Co(OH)_2/CC$ and (b) $Ru-Co(OH)_2/CC$ at varied potentials in Ar-saturated 1 M KOH solution with 2000 ppm NO_3^-. (c) Phase peak angles of $Co(OH)_2/CC$ and $Ru-Co(OH)_2/CC$ at 0.3 to -0.4 V *vs.* RHE. (d) Quasi *in situ* EPR trapping of hydrogen radicals. (e) OCP curves of $Ru-Co(OH)_2/CC$ and $Co(OH)_2/CC$ in Ar-saturated 1 M KOH and 2000 ppm NO_3^- was injected subsequently. *In situ* Raman spectra of (f) $Ru-Co(OH)_2/CC$ and (g) $Co(OH)_2/CC$ at different applied potentials in Ar-saturated 1 M KOH solution with 2000 ppm NO_3^-. (h) I_{1060}/I_{1554} for $Ru-Co(OH)_2/CC$ and $Co(OH)_2/CC$ at different applied potentials. (i) Proposed mechanism of NH_3 synthesis from the electrochemical reduction of NO_3^- over $Ru-Co(OH)_2/CC$.

The electronic structures of $Co(OH)_2$ and $Ru-Co(OH)_2$ were analyzed to elucidate the catalytic activity enhancement resulting from Ru doping. The electron location function (ELF) revealed increased localization near Ru atoms compared to $Co(OH)_2$, indicating stronger electron exchange between $Ru-Co(OH)_2$ and adsorbed NO_3^- (Fig. 4b). The density of states (DOS) analysis (Fig. 4c) demonstrated that Ru doping shifted the occupied electron states closer to the Fermi energy level, resulting in a higher DOS for $Ru-Co(OH)_2$. The d-band centers of $Co(OH)_2$ and $Ru-Co(OH)_2$ were -2.26 and -2.12 eV, respectively. This upward shift in the d-band center for $Ru-Co(OH)_2$ was primarily attributed to the enhanced electronic states of Ru d_{yz} and $d_{z^2-y^2}$ orbitals near the Fermi level (Fig. S39 and S40, ESI†). Based on the d-band center theory, a higher d-band center indicates stronger interactions with intermediates, highlighting the improved catalytic potential of $Ru-Co(OH)_2$.[51,52] The differential charge density and Bader charge analyses (Fig. 4d) further investigated the charge transfer processes

between Ru/Co and NO_3 species in $Co(OH)_2$ and $Ru-Co(OH)_2$. The results indicated a significant charge redistribution around Ru atoms at the $Ru-Co(OH)_2$ interface, with greater charge transfer to adsorbed NO_3^- compared to $Co(OH)_2$, Specifically, Co atoms in $Co(OH)_2$ transferred 0.39 electrons to nearby O atoms, while Ru atoms in $Ru-Co(OH)_2$ transferred a total of 1.02 electrons to the surrounding O atoms (Fig. S41, ESI†). Combined with ELF findings, this suggests that Ru atoms enhance interfacial electron aggregation and promote efficient transfer to adsorbed intermediates, boosting catalyst performance.

According to thermodynamic calculations, the adsorption free energy of NO_3^- on $Ru-Co(OH)_2$ was -2.95 eV, compared to -2.46 eV for $Co(OH)_2$, indicating that Ru doping improves the thermodynamic favorability of NO_3^- adsorption (Fig. S42, ESI†). Bader charge analysis verifies the higher oxidation states of the Co species in $Ru-Co(OH)_2$ (Fig. S43 and Table S3, ESI†). Additionally, Fig. 4e shows that the rate-determining step (RDS) for $Co(OH)_2$ in the NO_3RR is the transformation of $*NO_2$ into
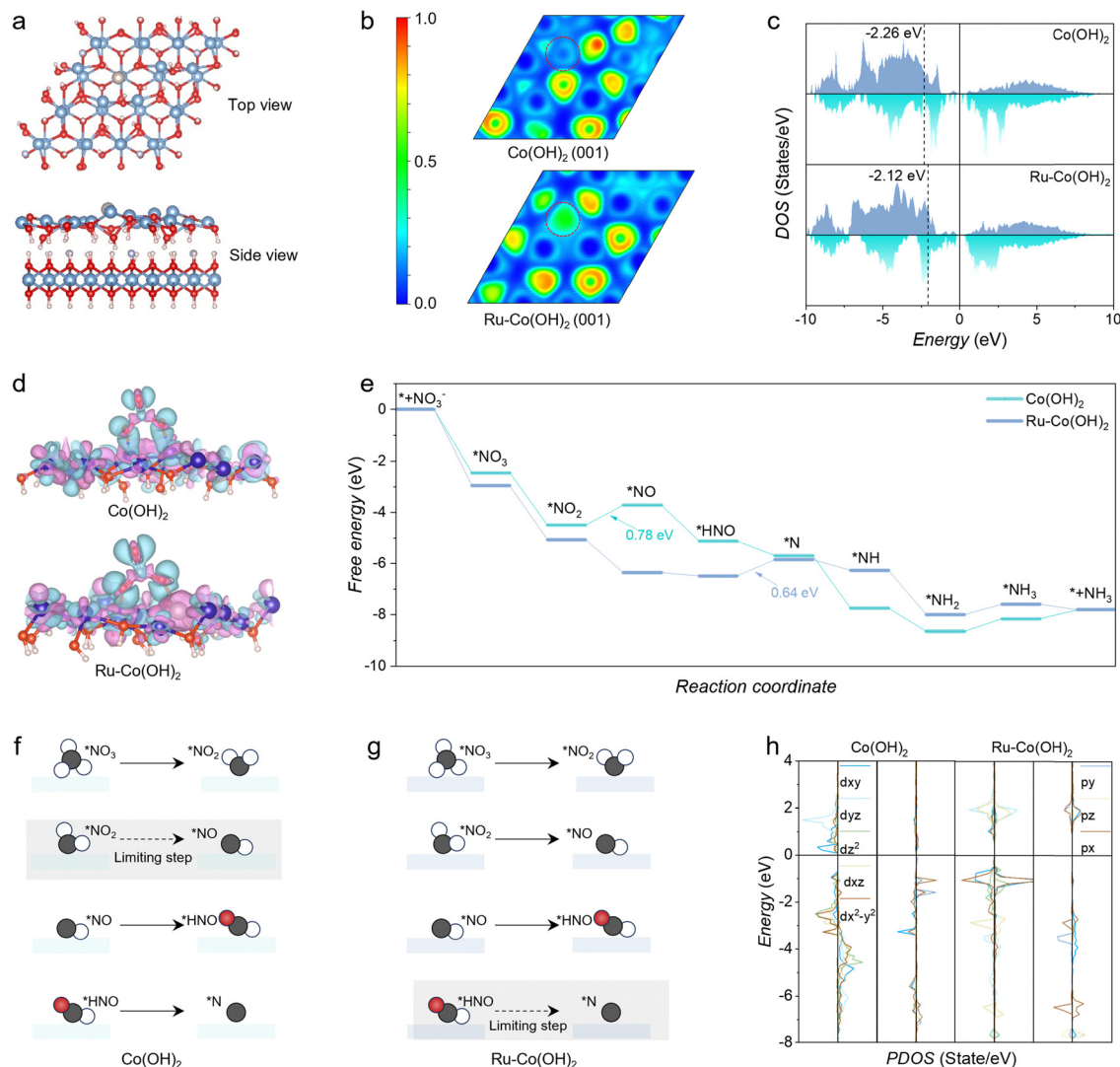
Fig. 4 Theoretical calculation analysis. (a) The top view (top) and side view (bottom) of the Ru–Co(OH)$_2$ model. (b) The electron location function and (c) density of states of Co(OH)$_2$ and Ru–Co(OH)$_2$. (d) Differential charge density of *NO$_3$ of Co(OH)$_2$ and Ru–Co(OH)$_2$. The isosurface value is set to be 0.02 e Å^{-3}, and the consumption and accumulation of charges are shown in yellow and cyan, respectively. (e) Reaction free-energy diagram of Co(OH)$_2$ and Ru–Co(OH)$_2$ for the NO$_3$RR. Schematic of the electrochemical NO$_3$RR toward NH$_3$ for (f) Co(OH)$_2$ and (g) Ru–Co(OH)$_2$. (h) Partial density of states of Co–N atoms and Ru–N atoms of the *HNO intermediate over Co(OH)$_2$ and Ru–Co(OH)$_2$.

*NO, with an energy barrier of 0.78 eV. In contrast, Ru doping alters the RDS to the transition from *HNO to *H, significantly reducing the energy barrier to 0.64 eV (Fig. S44 and S45, and Table S4, ESI†). This shift in the RDS implies that the accumulation of *HNO on Ru–Co(OH)$_2$, due to restricted *HNO dissociation, aligns with *in situ* Raman spectroscopy observations. DFT calculations were performed to assess the competitive hydrogen evolution reaction (HER) pathway on Ru–Co(OH)$_2$. As shown in Fig. S46–S48 (ESI†), the energy barrier for the HER step (*H → $\frac{1}{2}$H$_2$) is 1.29 eV, higher than the 0.64 eV for the NO$_3$RR rate-determining step. This suggests a kinetic preference for NO$_3^-$ reduction over the HER. Overall, the incorporation of Ru atoms modulates the electronic structure of the Co(OH)$_2$ active site, enhances electron transfer, improves NO$_3^-$ adsorption, and facilitates the conversion of *NO$_2$ intermediates. The incorporation of Ru significantly enhances the Ru–N

interaction in the *HNO intermediate, effectively modulating the reaction pathway and the RDS (Fig. 4f and g). The partial density of states (PDOS) analysis of the *HNO intermediate over Co(OH)$_2$ and Ru–Co(OH)$_2$ further elucidates the underlying mechanism. As shown in Fig. 4h, the d$_{xz}$ and d$_{yz}$ orbitals of Ru, in comparison with Co(OH)$_2$ exhibit substantial orbital coupling with the p$_x$ and p$_y$ orbitals of the N atoms in the unoccupied states ($\sim$2 eV). Moreover, in the occupied states ($\sim$−3 eV), the Ru d$_{xz}$ and d$_{yz}$ orbitals display strong coupling with the N p$_x$ and p$_y$ orbitals, respectively. This orbital coupling significantly enhances the adsorption stability of the *HNO intermediate on Ru–Co(OH)$_2$.

Potential industrial application

To demonstrate the industrial potential for the NO$_3$RR under ambient conditions, we assembled an NO$_3$RR-OER MEA

5628 | *Energy Environ. Sci.*, 2025, **18**, 5622–5631

This journal is © The Royal Society of Chemistry 2025

electrolyzer with Ru–Co(OH)$_2$/CC (2 × 2 cm^2) as the cathode and IrO$_2$ on platinum-coated titanium felt (IrO$_2$/PTF) (2 × 2 cm^2) as the anode (Fig. 5a). The PTF substrate was chosen for its excellent electrical conductivity and corrosion resistance, while the platinum coating mitigates the surface passivation of titanium, thereby ensuring stable interfacial conductivity during long-term operation.[53] The Ru–Co(OH)$_2$/CC‖IrO$_2$/PTF MEA exhibited significantly reduced resistance and achieved an industrial current density of 500 mA cm^{-2} at 2.6 V, markedly outperforming the Co(OH)$_2$/CC‖IrO$_2$/PTF device (~280 mA cm^{-2} at 2.6 V) (Fig. 5b and Fig. S49, ESI†). To ensure consistent NO$_3^-$ conversion, we optimized the flow rate (Fig. S50, ESI†). Using the MEA electrolyzer with Ru–Co(OH)$_2$/CC as the cathode, NO$_3^-$ was converted to NH$_3$ with a FE of 94 ± 6% and a yield rate of 7472 ± 487 µg h^{-1} cm$_{geo}^{-2}$ at 100 mA cm^{-2}, demonstrating excellent potential for NH$_3$ production (Fig. 5c and Fig. S51, ESI†). The stability of the MEA system was further investigated, and it maintained an average NH$_3$ FE of ~93%, an NH$_3$ yield rate of ~7000 µg h^{-1} cm$_{geo}^{-2}$, and a voltage of 1.9 V at 100 mA cm^{-2} for over 100 h (Fig. 5d). The minor voltage fluctuations observed are attributed to electrolyte replenishment, necessary to compensate for nitrate depletion and maintain consistent reaction conditions.

To confirm the practical potential for NH$_3$ production, a high-purity NH$_3$ product was collected after NO$_3^-$ electroreduction using an acid trap method (Fig. S52–S54, ESI†).[54] The successful production of NH$_4$Cl is confirmed by the XRD pattern in Fig. 5e and the related elemental mapping results in Fig. S55 (ESI†). Building on this promising performance, a TEA was conducted to evaluate the feasibility and the potential for commercialization (Note S1, ESI†). As shown in Fig. S56 (ESI†), the estimated total cost of NH$_3$ production using the MEA electrolyzer was approximately US$ 1.995 per kg NH$_3$. This system demonstrates high viability, particularly when considering the potential profitability of NO$_3^-$ wastewater treatment. The major cost contributions are the electricity consumption (39.12%), electrolytic cell (26.94%), and balance of plant (14.5%) (Fig. 5f). Optimizing the electrolyzer design and reducing electricity costs could significantly enhance the economic potential of converting NO$_3^-$ wastewater into NH$_3$. The TEA analysis used an industrial electricity price of US$0.03 kW h in this study,[55] and further cost reductions could be achieved by leveraging excess renewable energy from wind or solar sources. The relationship between the electricity cost and current density is illustrated in the contour map (Fig. 5g). Notably, if electricity costs drop below US$0.03 kW h in the future, the
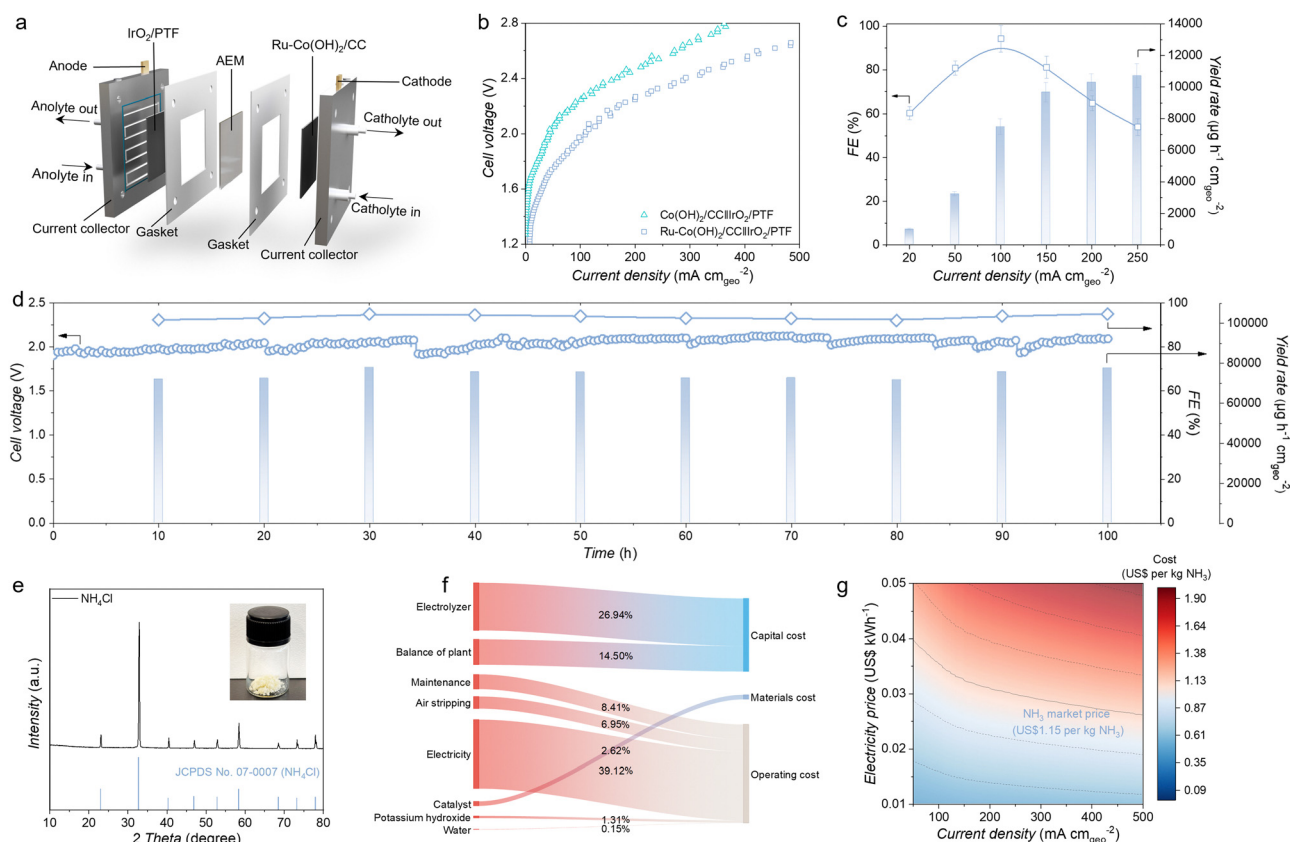

Fig. 5 Practical NH$_3$ product synthesis. (a) Schematic of a MEA cell for the NO$_3$RR. (b) Polarization curves of the MEA cell with Ru–Co(OH)$_2$/CC and Co(OH)$_2$/CC cathodes, paired with an IrO$_2$/PTF anode. (c) NH$_3$ FEs and yield rates of the Ru–Co(OH)$_2$/CC over a broad range of current densities in the MEA. (d) Stability of the MEA system at 100 mA cm^{-2}, tracking NH$_3$ FEs, yield rates, and the cell voltage using a Ru–Co(OH)$_2$/CC cathode and an IrO$_2$/PTF anode. (e) XRD pattern of the synthesized NH$_4$Cl product (the inset is the photograph of the synthesized NH$_4$Cl product). (f) Estimated costs for the NO$_3$RR in the MEA system. (g) Contour map illustrating NH$_3$ synthesis costs as a function of current densities and electricity prices.

This journal is © The Royal Society of Chemistry 2025

Energy Environ. Sci., 2025, **18**, 5622–5631 | **5629**

total cost of NH_3 production *via* this MEA system could fall below the current market price of NH_3 produced by the Haber–Bosch process (US$1.15 per kg NH_3)[56] at current densities below 300 mA cm^{-2}, even before accounting for additional profits from wastewater treatment.

Conclusions

In summary, we report the dynamic structural evolution of Ru–Co(OH)$_2$/CC as an efficient electrode for the NO$_3$RR, identifying Co(III) sites as the crucial active sites for NH_3 generation. The optimal Ru–Co(OH)$_2$/CC attains a high NH_3 FE of ∼96% and a large yield rate of ∼56 501 µg h^{-1} cm$_{geo}$$^{-2}$ in 1 M KOH solution with 2000 ppm NO$_3$$^-$. *Ex situ* XAS and XRD analyses reveal a dynamic evolution of Co(III) sites on the Ru–Co(OH)$_2$/CC during the NO$_3$RR. *In situ* Raman spectroscopy and EPR spectroscopy demonstrate that Ru doping facilitates the generation of hydrogen radicals, which promote the hydrogenation of *HNO intermediates on adjacent Co(III) sites. Economic modeling underscores the techno-economic feasibility of the NO$_3$RR, presenting it as a greener alternative for NH_3 synthesis and NO$_3$$^-$ wastewater treatment. This study not only provides an effective strategy to design and construct Co-based catalysts for the NO$_3$RR, but also unveils the crucial role of Co(III) sites for sustainable ammonia electrosynthesis.

Author contributions

L. Z., X. G., and Z. J. X. conceived the original concept and initiated the project. L. Z. wrote the manuscript. Y. L. carried out the theoretical calculations. L. Z. synthesized the materials and performed the characterization with assistance from S. X. (XAS), L. T. (XPS), J. Z. Y. S. (XRD), and S. S. (NMR). L. L. performed *in situ* Raman measurements. T. W., Q. W., X. L., K. T., and D. S. performed the data analysis. All authors contributed to the discussion of the manuscript.

Data availability

The data that support the findings in this study are available from the corresponding author upon reasonable request.

Conflicts of interest

There are no conflicts to declare.

Acknowledgements

References

1 C. H. Christensen, T. Johannessen, R. Z. Sørensen and J. K. Nørskov, *Catal. Today*, 2006, **111**, 140–144.

2 J. G. Chen, R. M. Crooks, L. C. Seefeldt, K. L. Bren, R. M. Bullock, M. Y. Darensbourg, P. L. Holland, B. Hoffman, M. J. Janik, A. K. Jones, M. G. Kanatzidis, P. King, K. M. Lancaster, S. V. Lymar, P. Pfromm, W. F. Schneider and R. R. Schrock, *Science*, 2018, **360**, eaar6611.

3 Mineral Commodity Summaries 2022 (US Geological Survey, 2022).

4 M. Wang, M. A. Khan, I. Mohsin, J. Wicks, A. H. Ip, K. Z. Sumon, C.-T. Dinh, E. H. Sargent, I. D. Gates and M. G. Kibria, *Energy Environ. Sci.*, 2021, **14**, 2535–2548.

5 L. Zhang, J. Liang, Y. Wang, T. Mou, Y. Lin, L. Yue, T. Li, Q. Liu, Y. Luo, N. Li, B. Tang, Y. Liu, S. Gao, A. A. Alshehri, X. Guo, D. Ma and X. Sun, *Angew. Chem., Int. Ed.*, 2021, **60**, 25263–25268.

6 W. Qiu, X.-Y. Xie, J. Qiu, W.-H. Fang, R. Liang, X. Ren, X. Ji, G. Cui, A. M. Asiri, G. Cui, B. Tang and X. Sun, *Nat. Commun.*, 2018, **9**, 3485.

7 X. Fu, V. A. Niemann, Y. Zhou, S. Li, K. Zhang, J. B. Pedersen, M. Saccoccio, S. Z. Andersen, K. Enemark-Rasmussen, P. Benedek, A. Xu, N. H. Deissler, J. B. V. Mygind, A. C. Nielander, J. Kibsgaard, P. C. K. Vesborg, J. K. Nørskov, T. F. Jaramillo and I. Chorkendorff, *Nat. Mater.*, 2024, **23**, 101–107.

8 B. H. R. Suryanto, H.-L. Du, D. Wang, J. Chen, A. N. Simonov and D. R. MacFarlane, *Nat. Catal.*, 2019, **2**, 290–296.

9 C. Tang and S.-Z. Qiao, *Chem. Soc. Rev.*, 2019, **48**, 3166–3180.

10 Y. Wang, C. Wang, M. Li, Y. Yu and B. Zhang, *Chem. Soc. Rev.*, 2021, **50**, 6720–6733.

11 J. Liang, Z. Li, L. Zhang, X. He, Y. Luo, D. Zheng, Y. Wang, T. Li, H. Yan, B. Ying, S. Sun, Q. Liu, M. S. Hamdy, B. Tang and X. Sun, *Chem*, 2023, **9**, 1768–1827.

12 H. Zhu, J. J. Wang, Z. Xu, Y. Tan and J. Wang, *Small*, 2024, **20**, 2404919.

13 G.-F. Chen, Y. Yuan, H. Jiang, S.-Y. Ren, L.-X. Ding, L. Ma, T. Wu, J. Lu and H. Wang, *Nat. Energy*, 2020, **5**, 605–613.

14 Y. Wang, A. Xu, Z. Wang, L. Huang, J. Li, F. Li, J. Wicks, M. Luo, D.-H. Nam, C.-S. Tan, Y. Ding, J. Wu, Y. Lum, C.-T. Dinh, D. Sinton, G. Zheng and E. H. Sargent, *J. Am. Chem. Soc.*, 2020, **142**, 5702–5708.

15 S. Sun, C. Dai, P. Zhao, S. Xi, Y. Ren, H. R. Tan, P. C. Lim, M. Lin, C. Diao, D. Zhang, C. Wu, A. Yu, J. C. J. Koh, W. Y. Lieu, D. H. L. Seng, L. Sun, Y. Li, T. L. Tan, J. Zhang, Z. J. Xu and Z. W. Seh, *Nat. Commun.*, 2024, **15**, 260.

16 Z.-Y. Wu, M. Karamad, X. Yong, Q. Huang, D. A. Cullen, P. Zhu, C. Xia, Q. Xiao, M. Shakouri, F.-Y. Chen, J. Y. Kim,

5630 | *Energy Environ. Sci.*, 2025, **18**, 5622–5631

This journal is © The Royal Society of Chemistry 2025

Y. Xia, K. Heck, Y. Hu, M. S. Wong, Q. Li, I. Gates, S. Siahrostami and H. Wang, *Nat. Commun.*, 2021, **12**, 2870.

17 P. Wang, C. Liu, L. Rao, W. Tao, R. Huang, P. Huang and G. Zhou, *Energy Environ. Sci.*, 2024, **17**, 6698–6706.

18 P. H. van Langevelde, I. Katsounaros and M. T. M. Koper, *Joule*, 2021, **5**, 290–294.

19 M. J. Ascott, D. C. Gooddy, L. Wang, M. E. Stuart, M. A. Lewis, R. S. Ward and A. M. Binley, *Nat. Commun.*, 2017, **8**, 1416.

20 Q. Liu, L. Xie, J. Liang, Y. Ren, Y. Wang, L. Zhang, L. Yue, T. Li, Y. Luo, N. Li, B. Tang, Y. Liu, S. Gao, A. A. Alshehri, I. Shakir, P. O. Agboola, Q. Kong, Q. Wang, D. Ma and X. Sun, *Small*, 2022, **18**, 2106961.

21 S. Liang, X. Teng, H. Xu, L. Chen and J. Shi, *Angew. Chem., Int. Ed.*, 2024, **63**, e202400206.

22 Q. Yan, R. Zhao, L. Yu, Z. Zhao, L. Liu and J. Xi, *Adv. Mater.*, 2024, **36**, 2408680.

23 X. Deng, Y. Yang, L. Wang, X.-Z. Fu and J.-L. Luo, *Adv. Sci.*, 2021, **8**, 2004523.

24 L. Qiao, A. Zhu, D. Liu, K. An, J. Feng, C. Liu, K. W. Ng and H. Pan, *Adv. Energy Mater.*, 2024, **14**, 2402805.

25 S. Han, H. Li, T. Li, F. Chen, R. Yang, Y. Yu and B. Zhang, *Nat. Catal.*, 2023, **6**, 402–414.

26 T. Wu, S. Sun, J. Song, S. Xi, Y. Du, B. Chen, W. A. Sasangka, H. Liao, C. L. Gan, G. G. Scherer, L. Zeng, H. Wang, H. Li, A. Grimaud and Z. J. Xu, *Nat. Catal.*, 2019, **2**, 763–772.

27 Y. Sun, J. Wang, S. Xi, J. Shen, S. Luo, J. Ge, S. Sun, Y. Chen, J. V. Hanna, S. Li, X. Wang and Z. J. Xu, *Nat. Commun.*, 2023, **14**, 2467.

28 T. Wu, Y. Sun, X. Ren, J. Wang, J. Song, Y. Pan, Y. Mu, J. Zhang, Q. Cheng, G. Xian, S. Xi, C. Shen, H.-J. Gao, A. C. Fisher, M. P. Sherburne, Y. Du, J. W. Ager, J. Gracia, H. Yang, L. Zeng and Z. J. Xu, *Adv. Mater.*, 2023, **35**, 2207041.

29 E. Fabbri, M. Nachtegaal, T. Binninger, X. Cheng, B.-J. Kim, J. Durst, F. Bozza, T. Graule, R. Schäublin, L. Wiles, M. Pertoso, N. Danilovic, K. E. Ayers and T. J. Schmidt, *Nat. Mater.*, 2017, **16**, 925–931.

30 L.-W. Jiang, Y. Huang, Y. Zou, C. Meng, Y. Xiao, H. Liu and J.-J. Wang, *Adv. Energy Mater.*, 2022, **12**, 2202351.

31 F. T. Haase, A. Bergmann, T. E. Jones, J. Timoshenko, A. Herzog, H. S. Jeon, C. Rettenmaier and B. R. Cuenya, *Nat. Energy*, 2022, **7**, 765–773.

32 Q. Zhou, Q. Bian, L. Liao, F. Yu, D. Li, D. Tang and H. Zhou, *Chin. Chem. Lett.*, 2023, **34**, 107248.

33 H. Jia, N. Yao, Z. Liao, L. Wu, J. Zhu, Y. Lao and W. Luo, *Angew. Chem., Int. Ed.*, 2024, **63**, e202408005.

34 X.-Z. Yue, P. Tang, X. Du, W.-J. Yi, Z.-Y. Liu, S.-J. Wang and S.-S. Yi, *ACS Appl. Mater. Interfaces*, 2023, **15**, 11621–11630.

35 H. Jin, K. Zhou, R. Zhang, H. Cui, Y. Yu, P. Cui, W. Song and C. Cao, *Nat. Commun.*, 2023, **14**, 2494.

36 S. Wang, Q. Jiang, S. Ju, C.-S. Hsu, H. M. Chen, D. Zhang and F. Song, *Nat. Commun.*, 2022, **13**, 6650.

37 Y. Fernández-Nava, E. Marañón, J. Soons and L. Castrillón, *Bioresour. Technol.*, 2008, **99**, 7976–7981.

38 C. Wei, S. Sun, D. Mandler, X. Wang, S. Z. Qiao and Z. J. Xu, *Chem. Soc. Rev.*, 2019, **48**, 2518–2534.

39 C. Wei, R. R. Rao, J. Peng, B. Huang, I. E. L. Stephens, M. Risch, Z. J. Xu and Y. Shao-Horn, *Adv. Mater.*, 2019, **31**, 1806296.

40 S. Garcia-Segura, M. Lanzarini-Lopes, K. Hristovski and P. Westerhoff, *Appl. Catal., B*, 2018, **236**, 546–568.

41 H. Xu, G. Xu, B. Huang, J. Yan, M. Wang, L. Chen and J. Shi, *Angew. Chem., Int. Ed.*, 2023, **62**, e202218603.

42 H. Du, T. Sun, M. Wang, Y. Tang, Y. Yu and J. Wang, *Chem. Commun.*, 2025, **61**, 5719–5730.

43 J. L. Gilbert and P. Khullar, *J. Electrochem. Soc.*, 2020, **167**, 021505.

44 J. Lv, A. Cao, Y. Zhong, Q. Lin, X. Li, H. B. Wu, J. Yan and A. Wu, *Nat. Commun.*, 2024, **15**, 6675.

45 Y. Feng, X. Wang, J. Ma, N. Wang, Q. Liu, K. Suenaga, W. Chen, J. Zhang, Y. Zhou and J. Wang, *Adv. Energy Mater.*, 2024, **14**, 2401501.

46 P. Zhou, X. Lv, S. Tao, J. Wu, H. Wang, X. Wei, T. Wang, B. Zhou, Y. Lu, T. Frauenheim, X. Fu, S. Wang and Y. Zou, *Adv. Mater.*, 2022, **34**, 2204089.

47 J. Yang, H. Liu, W. N. Martens and R. L. Frost, *J. Phys. Chem. C*, 2010, **114**, 111–119.

48 W. He, J. Zhang, S. Dieckhöfer, S. Varhade, A. C. Brix, A. Lielpetere, S. Seisel, J. R. C. Junqueira and W. Schuhmann, *Nat. Commun.*, 2022, **13**, 1129.

49 M. Xu, J. P. Larentzos, M. Roshdy, L. J. Criscenti and H. C. Allen, *Phys. Chem. Chem. Phys.*, 2008, **10**, 4793–4801.

50 Y. Ling, C. Mills, R. Weber, L. Yang and Y. Zhang, *J. Am. Chem. Soc.*, 2010, **132**, 1583–1591.

51 B. Hammer and J. K. Norskov, *Nature*, 1995, **376**, 238–240.

52 B. Hammer and J. K. Nørskov, *Surf. Sci.*, 1995, **343**, 211–220.

53 S. Zhang, Z. Wang, R. Zhang, Y. He and K. Cen, *Int. J. Hydrogen Energy*, 2023, **48**, 35463–35476.

54 M.-H. Yuan, Y.-H. Chen, J.-Y. Tsai and C.-Y. Chang, *Process Saf. Environ. Prot.*, 2016, **102**, 777–785.

55 Levelized cost and levelized avoided cost of new generation resources (EIA, 2020); **https://www.eia.gov/outlooks/aeo/pdf/electricity_generation.pdf**.

56 G. Schnitkey, *et al.* Fertilizer prices and company profits going into spring 2023. Farmdoc Daily, **https://farmdocdaily.illinois.edu/2023/02/fertilizer-prices-and-company-profits-going-into-spring-2023.html** (2023).

This journal is © The Royal Society of Chemistry 2025

Energy Environ. Sci., 2025, **18**, 5622–5631 | **5631**